

How to Incorporate External Fields in Analog Ising Machines

Robbe De Prins ^{*†1,2}, Jacob Lamers ^{*†2}, Peter Bienstman¹, Guy Van der Sande², Guy Verschaffelt², and Thomas Van Vaerenbergh³

¹Photonics Research Group, Ghent University – imec, Technologiepark-Zwijnaarde 126, 9052 Gent, Belgium

²Applied Physics Research Group, Vrije Universiteit Brussel, Pleinlaan 2, 1050 Brussels, Belgium

³Hewlett Packard Labs, Diegem, Belgium

Abstract

Ising machines (IMs) are specialized devices designed to efficiently solve combinatorial optimization problems (COPs). They consist of artificial spins that evolve towards a low-energy configuration representing a problem’s solution. Most realistic COPs require both spin-spin couplings and external fields. In IMs with analog spins, these interactions scale differently with the continuous spin amplitudes, leading to imbalances that affect performance. Various techniques have been proposed to mitigate this issue, but their performance has not been benchmarked. We address this gap through a numerical analysis. We evaluate the time-to-solution of these methods across three distinct problem classes with up to 500 spins. Our results show that the most effective way to incorporate external fields is through an approach where the spin interactions are proportional to the spin signs, rather than their continuous amplitudes.

1 Introduction

Combinatorial optimization problems lie at the heart of numerous computational challenges in disciplines

that range from industry to fundamental science. Some examples are problems in logistics [1], finance [2], biology [3, 4], job scheduling [5], and traffic flow regulation [6]. Many of these problems are non-deterministic polynomial-time (NP) complete, making it exceptionally challenging to develop efficient algorithms to solve them. Today, such problems are demanding vast amounts of energy, with high-performance computing centers persistently dedicating substantial resources to them [7].

One promising solution is the use of specialized hardware rather than general-purpose digital computers. More specifically, there has been a surge of interest in Ising machines (IMs): hardware implementations designed to find low-energy states of the Ising model, defined by the following Hamiltonian:

$$\mathcal{H}(\{\sigma_i\}) = -\frac{1}{2} \sum_{i,j}^N J_{ij} \sigma_i \sigma_j - \sum_i^N h_i \sigma_i. \quad (1)$$

Here, $\sigma_i \in \{-1, 1\}$ are Ising spins, and N is the total number of spins. J_{ij} and h_i denote the real-valued strengths of the spin couplings and external fields, respectively.

It has been shown that it is possible to formulate any problem within the NP complexity class as an Ising model with only polynomial overhead [8, 9]. The ground state, i.e. the configuration of binary spins with the lowest energy according to Eq. (1),

^{*}These authors contributed equally.

[†]Correspondence and requests should be addressed to R.D.P (email: robbe.deprins@ugent.be) or to J.L. (email: Jacobus.Stijn.T.Lamers@vub.be).

then corresponds to the optimal solution of the optimization problem.

Many IM implementations have been proposed so far [10]. Some implementations are constructed using spins that are intrinsically *binary*, such as implementations based on quantum annealing [11], probabilistic p-bits [12, 13], spatial light modulators [14], and memristor Hopfield neural networks [15]. Others utilize *analog spins*, which take continuous values while satisfying constraints that enforce both the COP structure and spin bistability. Examples are Ising machines based on degenerate optical parametric oscillators [16, 17], opto-electric oscillators [18], electrical resonators [19], memristor crossbar arrays [20], and polariton condensates [21, 22]. In this paper, we focus on Ising machines with analog spins.

In general, analog IMs are modeled by a set of differential equations. The time evolution of the amplitude of spin i , denoted $s_i \in \mathbb{R}$, is described as:

$$\frac{ds_i}{dt} = \mathcal{F}_i(s_i, \alpha, \beta I_i), \quad (2)$$

where \mathcal{F} is a nonlinear function, α is the linear gain, β is the interaction strength. I_i is the local field of spin i , which can be modeled as follows:

$$I_i = \sum_j J_{ij} s_j + h_i. \quad (3)$$

The IM's energy, as given by Eq. (1), can be evaluated with spin amplitudes mapped to binary spins via $\sigma_i = \text{sgn}(s_i)$, where $\text{sgn}(\cdot)$ denotes the sign function.

While some studies have considered tasks that require external fields [23–28], the emphasis in benchmarking IMs (both with binary and analog spins) remains largely on problems that do not require such fields, such as the Max-Cut problem [29]. This focus contrasts with the requirements of most industrially relevant COPs, which necessitate external fields for their encoding into an IM [30].

For IMs with analog spins, implementing external fields can be challenging. This is clear from Eq. (3), where as the spin amplitudes decrease, the spin coupling terms ($\propto J_{ij} s_j$) are weakened relative to the external fields ($\propto h_i$), potentially causing the latter to dominate. Conversely, when spin amplitudes exceed one, the couplings may dominate instead. Since

embedding a COP into an IM requires careful tuning of the values of J_{ij} and h_i , such imbalances may undermine the IM's performance.

In the past, various techniques have been proposed to mitigate this issue [26, 27], but their impact on the IM's performance has not yet been benchmarked. In this work, we address this gap by conducting a numerical study. Moreover, we include an alternative method that substitutes $J_{ij} s_j$ for $J_{ij} \text{sgn}(s_j)$ in Eq. (3). This method was originally proposed for ballistic simulated bifurcation [31, 32], a specific type of analog IM where \mathcal{F} in Eq. (2) is a *linear* function (whereas a nonlinear function is used in this work) and spins evolve with momentum rather than following a gradient method. While this binarization method is uncommon in other analog IMs [10] and has not been included in earlier studies of imbalances between spin couplings and external fields [33], we will show that it is particularly effective for incorporating external fields and outperforms the previously proposed techniques.

We apply all methods to three different problem classes, each requiring a distinct mapping to embed problems into an Ising machine: (a) Sherrington–Kirkpatrick (SK) Hamiltonians with random external fields, which we generated ourselves, (b) quadratic unconstrained binary optimization (QUBO) problems from BiqMac's Beasley benchmark set [34], and (c) Max-3-Cut problems, where graphs are generated using the Rudy generator [35]. While SK problems serve as a general benchmark—sampling J_{ij} and h_i from Gaussian distributions rather than relying on a structured mapping—the other two classes represent typical ways external fields emerge in problem embeddings (see Results for details).

In addition to the techniques discussed above, we also explore a simple recalibration of the external fields by rescaling them with a constant factor, i.e. replacing h_i by ζh_i in Eqs. (1) and (3) where $\zeta \in \mathbb{R}$. This adjustment essentially modifies the embedding process of COPs and can be easily combined with any of the prior methods. This constant rescaling has been proposed in previous works [27, 33], where it was suggested to enhance the performance of IMs. In this work, we show that such a constant rescaling can

indeed be necessary when encoding COPs with soft constraints, such as for Max-3-Cut problems. However, for COPs without such constraints, such as in the SK and Beasley problems, this rescaling removes the guarantee that the ground-state spin configuration solves the COP, resulting in an incorrect COP embedding.

2 Modeling analog Ising machines

2.1 Transfer function

Ising machines with analog spins rely on nonlinear dynamics to establish bistable spin amplitudes. This bistability is typically realized through a pitchfork bifurcation, which can be achieved via different nonlinear functions \mathcal{F} in Eq. (2). A prior study compared many nonlinear functions [36], and showed that the following nonlinearity achieves the best performance:

$$\frac{ds_i}{dt} = -s_i + \tanh(\alpha s_i + \beta I_i). \quad (4)$$

This nonlinearity is commonly employed to incorporate the saturation of the spin amplitudes, often observed in experimental setups [18]. Its good performance can be attributed to its inherent suppression of amplitude inhomogeneity, a common source of error when mapping COPs to IMs with analog spins. Moreover, this nonlinearity is particularly well-suited when external fields are present. Indeed, as described in the introduction, external fields ($\propto h_i s_i$) dominate over the spin couplings ($\propto J_{ij} s_i s_j$) when spin amplitudes are small ($s_i \ll 1$). Conversely, spin couplings dominate when the spin amplitudes exceed one. Eq. (4) now constrains the spin amplitudes to the range $[-1, 1]$, thereby excluding the latter scenario. For these reasons, the remainder of this work exclusively considers the hyperbolic tangent nonlinearity.

2.2 Annealing scheme

At the start of a simulation of the IM, the spin amplitudes are initialized near zero, and their evolution is

tracked over time by numerically integrating Eq. (4). Specific details are provided in Supplementary Note 1. The interaction strength β is increased at each timestep, following a commonly used linear annealing scheme [37, 38]:

$$\beta(t) = \beta_0 + v_\beta t. \quad (5)$$

Here, β_0 is the initial β -value and v_β is the annealing speed. As also detailed in Supplementary Note 1, we choose a relatively low and constant noise strength while integrating Eq. (4).

2.3 Methods to incorporate external fields

In this manuscript, we will compare the performance of four methods for incorporating external fields, which we outline below. For each of these methods, we will illustrate the spin dynamics using a 3-spin COP, which is visualized in Fig. 1(a), and for which the ground state configuration is $(-1, 1, -1)$.

2.3.1 The original external fields

All considered methods essentially modify the local field of spin i , as originally defined by Eq. (3). Hence, we will further refer to Eq. (3) as the ‘original external fields’. For the 3-spin COP of Fig. 1(a), the evolution of the spin amplitudes under Eqs. (3) to (5) is visualized in Fig. 1(b) where $\beta_0 = 0$. As we start to increase β , the spins initially follow the dotted lines. As shown in Supplementary Note 2, these dotted lines correspond to $\frac{ds_i}{d\beta} = \frac{h_i}{1-\alpha}$, such that the spin dynamics at low β are determined by the external fields h_i , independent of the spin couplings J_{ij} . As the amplitudes grow, the spin couplings strengthen (the first term in Eq. (3) grows), causing spin 2 to flip and leading to the ground state configuration $(-1, 1, -1)$.

Thus, for this simple COP, the IM successfully overcomes the initial field-driven behavior. However, for more complex problems, this may not always be the case. As discussed in Section 1, an imbalance between the spin couplings and the external fields can undermine the validity of the COP embedding.

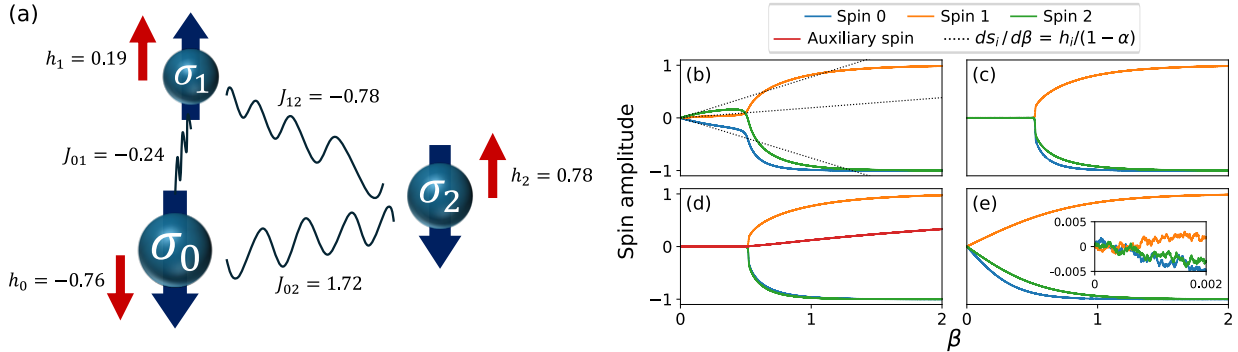


Figure 1: (a) Example of a 3-spin COP with ground state configuration $(-1, 1, -1)$. (b)-(e) Spin evolution under the methods described in Eqs. (3) and (6) to (8), respectively. In (b), the initial direction of the spins (dotted lines) is given by $h_i/(1 - \alpha)$, independently of the spin-spin couplings J_{ij} . Methods in (c)-(e) are designed to prevent the external fields from dominating the spin-spin couplings. The inset in (e) shows a zoom-in near $\beta = 0$.

2.3.2 The mean absolute spin method

One way to address the imbalance between spin couplings and the external fields is to rescale the external fields with the mean of the absolute values of the spin amplitudes [27], leading to the following local field:

$$I_i = \sum_{j=1}^N J_{ij} s_j + h_i \frac{1}{N} \sum_k |s_k|. \quad (6)$$

This approach ensures that the external field terms scale linearly with the spin amplitudes, consistent with the scaling of the spin couplings.

Fig. 1(c) shows the evolution of the spins following this approach. We observe that the spin amplitudes remain zero until they bifurcate into the ground-state solution. Hence, this method prevents the external fields from dominating over the spin couplings.

We observe that the origin ($s_i = 0, \forall i$) is a stable fixed point up to a certain β value, at which the spins bifurcate. Ideally, β_0 would be set equal to this critical value. However, as explained in Supplementary Note 3, determining this exact value is challenging, and we further choose to set $\beta_0 = 0$ when using the mean absolute spin method. Although a heuristic could, in principle, estimate β_0 more accurately and potentially improve performance, we do not explore that direction here. As shown in Supplementary Note

3, the choice of β_0 has only a moderate effect and does not influence our conclusions in the remainder of this work.

2.3.3 The auxiliary spin method

An alternative method to rescale the external fields is provided by the ‘auxiliary spin method’ [26]. It introduces an auxiliary spin amplitude s_{N+1} , and replaces each external field h_i by a coupling between spin i and the auxiliary spin. The local field of spin i is modified as follows:

$$I_i = \begin{cases} \sum_{j=1}^N J_{ij} s_j + h_i s_{N+1}, & \text{if } i < N + 1, \\ \sum_{j=1}^N h_j s_j, & \text{if } i = N + 1, \end{cases} \quad (7)$$

$$= \sum_{j=1}^{N+1} J'_{ij} s_j, \quad \text{where } \mathbf{J}' = \begin{bmatrix} \mathbf{J} & \mathbf{h} \\ \mathbf{h}^T & 0 \end{bmatrix}.$$

Hence, applying this technique only requires the implementation of spin couplings.

It can be shown that if \mathbf{s}_{opt} is the optimal solution to the original Ising problem of Eq. (1), then $(\mathbf{s}_{\text{opt}}, 1)$ and $(-\mathbf{s}_{\text{opt}}, -1)$ are degenerate solutions of the system with the auxiliary spin [26]. Hence, if the auxiliary spin amplitude takes a negative value, all spins are flipped before evaluating the IM’s energy via Eq. (1).

Fig. 1(d) illustrates the evolution of the spins using this method. Similar to the mean absolute spin approach, the spin amplitudes remain zero until they bifurcate into the ground-state solution. However, for the auxiliary spin method, we show in Supplementary Note 4 that the β -value at this bifurcation can be easily calculated, allowing us to set β_0 to this value.

2.3.4 The spin sign method

The spin sign method [31, 32] defines the local field of spin i as follows:

$$I_i = \sum_j J_{ij} \text{sgn}(s_j) + h_i. \quad (8)$$

Fig. 1(e) shows the evolution of the spins following this approach where we set $\beta_0 = 0$. The inset provides a more detailed view near β_0 . For this simple COP, we observe that the spin sign method first explores the surroundings of the origin. Once the signs of the spins correspond to the COP’s solution, the local fields remain at constant values such that the spin amplitudes continue to grow linearly until they saturate.

2.4 Scaling external fields by a constant

Previous works have proposed to rescale the external fields by a constant $\zeta \in \mathbb{R}$ [27, 33], thereby substituting h_i for ζh_i in Eqs. (3) and (6) to (8). However, these works did not provide any insights into why this rescaling technique should be adopted and for which COPs it is effective.

Embedding a COP into an IM determines the values of J_{ij} and h_i . For many COPs, such as SK problems and Beasley problems, this embedding guarantees that the ground-state of Eq. (1) corresponds to a solution of the COP. Hence, it is counterintuitive to set $\zeta \neq 1$, since this modifies the energy landscape of Eq. (1), thereby eliminating this guarantee. For example, if we substitute h_i with ζh_i in Eq. (1) and set $\zeta \gg 1$, the external fields dominate the system, resulting in a ground-state configuration $\text{sgn}(h_i)$. In

this scenario, the spin couplings – which encode information that is essential to solving the COP – are effectively disregarded.

For some problems, such as Max-3-cut, so-called soft constraints are used to embed a COP. These constraints are implemented by adding terms to the energy function of Eq. (1), such that violating these constraints incurs an energy penalty. These terms come with a prefactor that indicates the importance of the corresponding constraint. However, when using soft constraints, the ground-state configuration will only solve the COP if the prefactors of all constraints are set to appropriate values. Specifically, for Max-3-Cut problems, we will demonstrate that determining the correct prefactor is challenging for realistically-sized COPs, but surprisingly, this issue can be resolved by applying a factor $\zeta \approx 0.6$.

3 Results

In this section, we discuss the performance of the rescaling techniques introduced in the previous section. We do this using three different problem classes, which are introduced in the following subsections.

The IM’s performance is evaluated using the time-to-solution (TTS) metric, which represents the total time needed to reach the target state with 99% probability. It is defined as:

$$\text{TTS} = \begin{cases} T, & \text{if } P > 0.99, \\ T \frac{\log(0.01)}{\log(1-P)}, & \text{if } 0 < P \leq 0.99, \\ \infty, & \text{if } P = 0, \end{cases} \quad (9)$$

where P is the probability of reaching the target state, and T is the (dimensionless) time window over which Eq. (4) is integrated. Whenever possible, the ground state is chosen as the target. When the ground state is unknown, a target energy is chosen corresponding to the best-known solution, as detailed in later sections.

Whereas T is typically treated as a hyperparameter [39], which leads to the performance measure $\min_T \text{TTS}(T, P(T))$, here we choose to set T as the average simulation time required to reach the target state across successful runs. This choice provides a

practical approximation of the TTS, as it demands fewer computational resources for evaluation, compared to treating T as a hyperparameter. We estimate the values of P and T over 100 runs.

The performance of the IM depends on the choice of the linear gain α and the annealing speed v_β (cf. Eqs. (4) and (5)). Given a COP and a method from Section 2.3, these hyperparameters are optimized, and the corresponding value of \min_{α, v_β} TTS is reported. For the Max-3-Cut problems, an additional hyperparameter specific to the Ising formulation is optimized (see later). Unless stated otherwise, the constant rescaling factor ζ , introduced in Section 2.4, is set to 1. Where relevant, it is treated as an additional hyperparameter. Further details about the hyperparameter optimization procedure are provided in the Supplementary Note 1.

3.1 Sherrington–Kirkpatrick Hamiltonians with random external fields

The first type of problem we consider is a Sherrington-Kirkpatrick (SK) spin glass. The goal of this task is to find the configuration of binary spins $\sigma_i \in \{-1, 1\}$ that minimizes the Hamiltonian in Eq. (1), where the elements of the coupling matrix are drawn from a Gaussian distribution [40] (with zero mean and standard deviation 1). We extend the SK spin glass model with external fields that are drawn from the same Gaussian distribution.

We considered problems with 50, 100, 150, and 200 spins, generating 10 instances for each size. For problems with 50 spins, the ground state was obtained via an exact solver [41]. The larger problems could not be solved using this exact solver with our computational resources. Therefore, we used the state-of-the-art approximate solver PySA, which is based on simulated annealing with parallel tempering [42]. The parameters used can be found in Supplementary Note 5. The energies obtained by this solver are equal to the lowest energies found by the Ising machine for problems with 100 and 150 spins. However, for the problems with 200 spins, the Ising machine sometimes finds lower energies than PySA. Therefore, we define the

lowest energy found by the Ising machine (across all methods of Section 2.3) as the target energy. Since our primary focus is on the relative comparison of different methods for implementing external fields, this choice has no impact on the validity of our conclusions.

Fig. 2 compares the various methods of Section 2.3 in terms of TTS when solving SK problems. Each subfigure compares two methods. Each dot on the plot represents a problem. The x (y)-coordinate of a dot is the TTS when the problem is solved using the method on the horizontal (vertical) axis. Hence, the diagonal line represents the situation where both methods have the same TTS. A dot in the upper left (lower right) of figure denotes a problem that is solved faster by the method on the horizontal (vertical) axis.

Fig. 2(a) compares the original external field method of Eq. (3) with the spin sign method of Eq. (7). 22 of the 40 COPs are positioned in the grey region on the right, indicating $TTS = \infty$ when using the original external fields. This means that for each of these 22 problems and across all tested hyperparameter values, the original external fields failed to reach the target energy in all 100 runs within the maximum time of $t_{\max} = 10^4$ (cf. Eq. (9)). In contrast, the spin sign method successfully solved these instances, yielding a finite TTS. The remaining 18 COPs could be solved by either of the two methods. 14 of them were solved faster by the original external fields, while 4 were solved faster using the spin sign method.

In both Fig. 2(b) and (c), one of the 40 problems appears in the grey region on the right. Although not visible in the plots, this data point corresponds to the same COP, which could only be solved by the spin sign method, while the other three methods failed.

Fig. 2(b) and (c) appear similar, but Fig. (c) has more dots below the diagonal, indicating that the auxiliary spin method is generally faster than the mean absolute spin method.

In Supplementary Note 10, we provide the values of the success rate and the average runtime T of successful runs corresponding to the TTS values of Fig. 2.

Overall, the spin sign method performs best for the SK problems. While it solves all considered COPs, the original external fields fail on more than half.

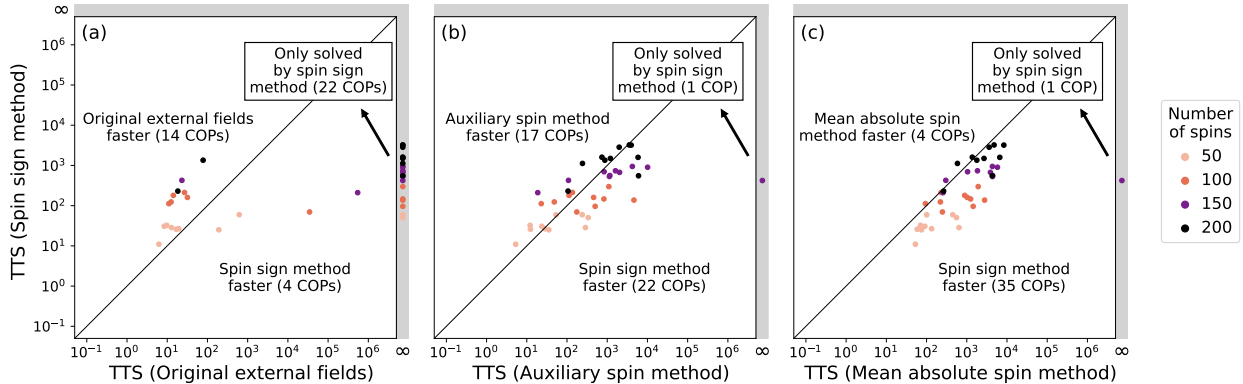


Figure 2: Comparison of time-to-solution between different methods to implement external fields (Eqs. (3) and (6) to (8)) for SK Hamiltonians with random external fields. Dots in the grey area on the right denote COPs that could be solved by the spin sign method within the allocated compute time of $t_{\max} = 10^4$, but not by the method on the x-axis ($TTS = \infty$, $SR = 0$). The spin sign method can solve more problems within the allocated time than the other methods, and it generally requires less time to do so.

Both the auxiliary spin method and the mean absolute spin method solve all but one COP; however, the latter is generally slower, while the former is only slightly slower than the spin sign method on average, making it the second-best-performing for these problems.

As discussed in Section 2.4, previous works proposed to scale external fields by a constant factor $\zeta \in \mathbb{R}$. Ref. [33] indicates that the IM’s performance, averaged over SK problems with at most 16 spins, is highly sensitive to the choice of ζ . However, in the Supplementary Note 6, we show that this sensitivity is due to the small problem size. Our results indicate that applying a scaling factor different from 1 is generally not beneficial here, reinforcing that $\zeta = 1$ is the best choice for solving SK problems. This is explained by the fact that setting $\zeta \neq 1$ removes the guarantee that the ground state spin corresponds to the problem’s optimal solution.

3.2 Quadratic unconstrained binary optimization problems

The problems analyzed in this section are the Beasley instances from the BiqMac library [34]. These are ex-

amples of quadratic unconstrained binary optimization (QUBO) problems, meaning that they are defined using binary variables $x_i \in \{0, 1\}$. Given a symmetric matrix Q , the goal is to find the configuration \mathbf{x} that minimizes the objective function $\mathbf{x}^T Q \mathbf{x}$.

These problems can be mapped to the Ising model using the following transformation:

$$x_i = \frac{\sigma_i + 1}{2}. \quad (10)$$

While the original QUBO formulations of these problems include only quadratic terms ($\propto x_i x_j$), Supplementary Note 7 shows that applying Eq. (10) results in both spin couplings ($\propto \sigma_i \sigma_j$) and external fields ($\propto \sigma_i$). Many COPs of interest are naturally defined as QUBO problems, making the transformation of Eq. (10) a common mechanism that gives rise to external fields in IMs.

The ground state energies for Beasley problems with up to 250 spins are provided in the BiqMac library [34]. For problems with 500 spins, the exact ground state is not known. For these problems, we use the upper bounds provided in the BiqMac library [34] as target values.

Fig. 3 compares the various methods to incorporate external fields, as defined in Section 2.3, in

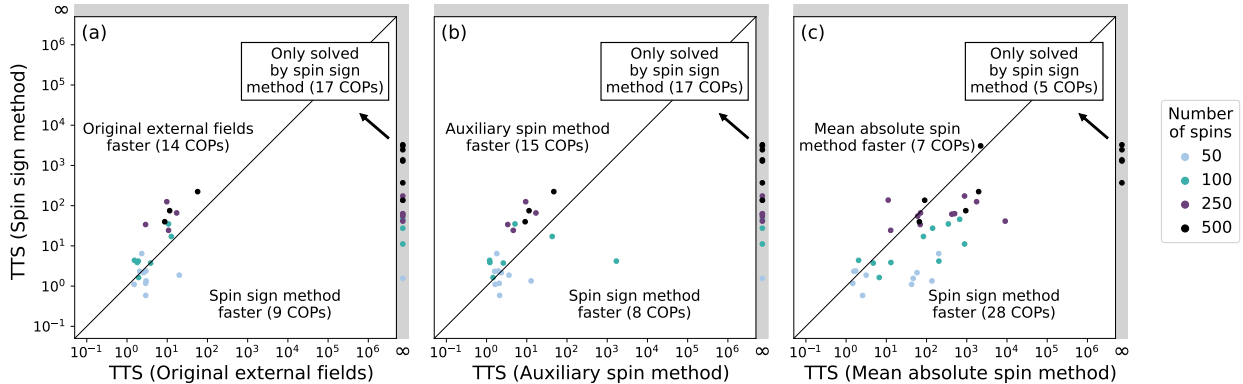


Figure 3: Comparison of time-to-solution between different methods to implement external fields for Beasley problems. Dots in the grey area on the right denote COPs that could be solved by the spin sign method within the allocated compute time of $t_{\max} = 10^4$, but not by the method on the x-axis ($TTS = \infty$, $SR = 0$).

terms of TTS, when applied to the Beasley problems. Fig. 3(a) compares the original external fields of Eq. (3) to the spin sign method of Eq. (8). 17 of the 40 COPs appear at the rightmost edge of the plot, indicating that they could not be solved using the original external fields, while they could be solved using the spin sign method.

Fig. 3(b) compares the auxiliary spin method of Eq. (7) with the spin sign method of Eq. (8). The plot looks similar to Fig. 3(a), and our results indicate that the same 17 COPs at the right edge of Fig. 3(a) could also not be solved using the auxiliary spin method.

Fig. 3(c) compares the mean absolute spin method of Eq. (6) with the spin sign method of Eq. (8). This time, only 3 COPs of the 40 could be solved exclusively by the spin sign method. Looking at the COPs that could be solved using either of the two methods, which are displayed in the white region of the plot, we see that the spin sign method generally reaches a solution faster.

Overall, we conclude from Fig. 3 that the spin sign method performs best as it can solve more Beasley problems than the other methods. The mean absolute spin method is the second-best-performing method as it solves more COPs than the original external fields and the auxiliary spin method. The

latter two methods yield comparable performance.

As explained in Section 2.4, it has been proposed in the past to multiply the external fields by a constant factor, but this removes the guarantee that the ground state spin configuration solves these problems. In Supplementary Note 6, we demonstrate that applying a factor different from 1 is generally not beneficial for Beasley problems, consistent with our findings for SK problems.

3.3 Max-3-Cut problems

The goal of the Max-3-Cut problem is to partition the vertices of an undirected graph into three sets, maximizing the number of edges that connect different sets, i.e. maximizing the so-called cut-value. In other words, we seek the best possible vertex coloring using 3 colors. In this section, we consider graphs generated using the rudy generator [35]. To benchmark the IM’s performance, the problems are solved to optimality using the publicly available `max_k_cut` package [41].

Max-3-Cut serves as a fundamental example of a COP requiring multivariate integer variables. Such problems are native to the Potts model, an extension of the Ising model, and are typically embedded in an Ising machine using one-hot encoding. This encoding

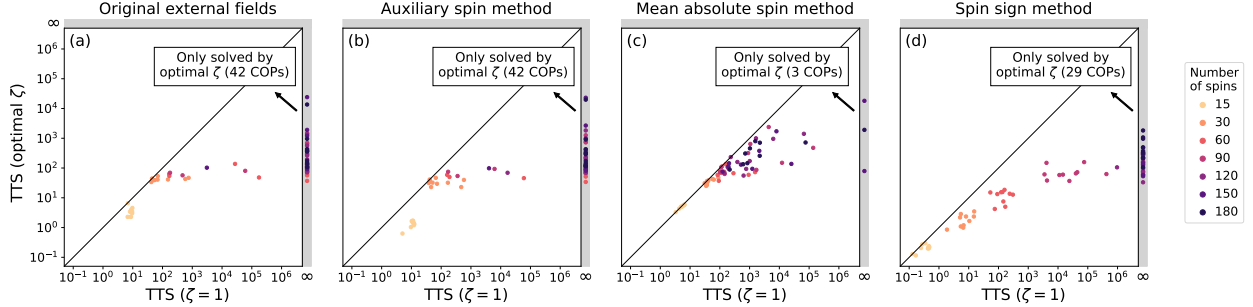


Figure 4: Comparison of time-to-solution between $\zeta = 1$ and the optimal ζ that minimizes the TTS, for each of the methods, for Max-3-Cut problems. Data points in the grey area on the right denote COPs that could not be solved using $\zeta = 1$ ($TTS = \infty$, $SR = 0$), given the allocated compute time of $t_{\max} = 10^4$.

introduces external fields, as will be explained in the next section.

3.3.1 Ising formulation

We utilize the Max-3-Cut Ising formulation as described in Ref. [30]. We denote the sets of vertices and edges in the graph as V and E respectively. For every vertex $v \in V$, a triplet of binary variables is introduced: $x_{v,i}$ where $i \in \{1, 2, 3\}$. $x_{v,i}$ equals 1 if vertex v has color i , and 0 otherwise. The energy is defined as follows:

$$\mathcal{H} = A \sum_{v \in V} \left(1 - \sum_{i=1}^3 x_{v,i} \right)^2 + B \sum_{(uv) \in E} \sum_{i=1}^3 x_{u,i} x_{v,i}, \quad (11)$$

where A and B are positive scalars. The first term enforces that all variable triplets $\{x_{v,1}, x_{v,2}, x_{v,3}\}$ are one-hot encoded since this positive term only vanishes if every triplet contains a single 1 and two 0's, ensuring the vertex colors are well-defined. The second term enforces the maximization of the cut value since an energy penalty is added for every edge that connects vertices with the same color. The ratio B/A denotes the relative importance of the two constraints.

The binary variables in Eq. (11) can be transformed to Ising spins using Eq. (10). As detailed in Supplementary Note 7, this allows us to rewrite

the energy as follows:

$$\mathcal{H} = \frac{A}{4} \sum_v \sum_{i \neq j} \sigma_{v,i} \sigma_{v,j} + \frac{B}{4} \sum_{(uv) \in E} \sum_{i=1}^3 \sigma_{u,i} \sigma_{v,i} + \zeta \sum_v \sum_{i=1}^3 \left(\frac{A}{2} + \frac{B}{4} \deg(v) \right) \sigma_{v,i}, \quad (12)$$

where $\deg(v)$ denotes the degree of vertex v . Note that we multiplied the external fields ($\propto \sigma_{v,i}$) by $\zeta \in \mathbb{R}$. Whereas Eqs. (11) and (12) are only strictly equivalent when $\zeta = 1$, we will show in the next section that setting $\zeta \neq 1$ is a necessary modification for the IM to achieve good performance.

3.3.2 Scaling external fields by a constant counters mapping errors

As explained in Section 2.4, it is generally not expected that rescaling the external fields with $\zeta \neq 1$ will improve the performance of an IM. Such a rescaling can eliminate the guarantee that the ground-state configuration solves the COP in question. In the previous sections, we confirmed that ζ is generally best put to 1 when solving an SK problem or Beasley problem.

However, we will show now that this is not the case for the Max-3-Cut mapping of Eq. (12). The inspiration for this approach comes from Ref. [27], which found that setting $\zeta \approx 0.6$ is optimal for a structure-based drug design problem of which the mapping also

contains one-hot encoding constraints and edge constraints, similar to Eq. (12), along with additional external fields. While the usefulness of this rescaling was observed, its underlying reasons were not explained. In this section, we will clarify why this rescaling works for Max-3-Cut.

First, we show that all implementation methods for external fields from Section 2.3 fail when $\zeta = 1$, but not when $\zeta \approx 0.6$. For each of these methods, Fig. 4 compares the case where ζ is fixed at 1 to the case where ζ is optimized within $[0, 1.2]$. In other words, the x-axis represents $\min_{\alpha, v_\beta, \frac{B}{A}} \text{TTS}$ for $\zeta = 1$, while the y-axis represents $\min_{\alpha, v_\beta, \frac{B}{A}, \zeta} \text{TTS}$. As expected, all points lie on or below the diagonal, since tuning ζ can only maintain or improve performance relative to fixing $\zeta = 1$. Across all four methods, several problems fall into the gray region on the right side of the figure. These instances cannot be solved with $\zeta = 1$ but become solvable when ζ is optimized within $[0, 1.2]$. Many of the remaining points show that optimizing ζ can yield improvements in TTS by several orders of magnitude.

Fig. 5 shows the optimal value of ζ as a function of the graph size. Each data point denotes the average optimal value across 10 problems of the same size. The standard deviation is represented by a shaded area. For all four rescaling methods, the optimal value of ζ converges to approximately 0.6. Although the optimal ζ may deviate from 0.6 in some cases, fixing $\zeta = 0.6$ generally yields comparable performance to using the instance-specific optimal value, as shown in Supplementary Note 8. This is not the case for other fixed values such as $\zeta = 0.4$ or $\zeta = 0.8$, which tend to result in worse performance.

This result is consistent with a prior study that identified $\zeta = 0.6$ as the optimal value for a similar problem that also uses one-hot encoding, but with $k > 3$ [27] (recall that $k = 3$ here). This suggests that the value $\zeta = 0.6$ holds for a broader class of problems using one-hot encoding.

We now show that the reason why this rescaling is necessary stems from the structure of Eq. (12). As explained in Section 2.4, the ground state configuration of a mapping that contains soft constraints will only solve the COP under consideration when the pref-

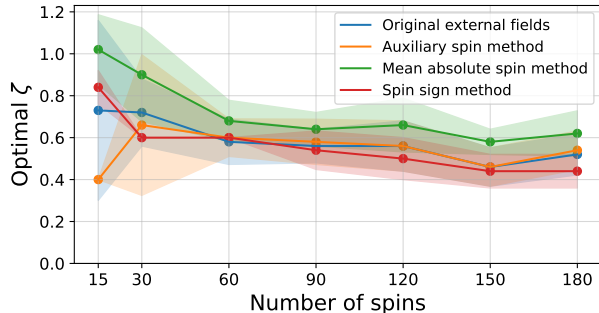


Figure 5: Optimal ζ values (which minimize TTS) as a function of the number of spins. Each dot represents the mean optimal value across 10 Max-3-Cut problems. Shaded areas represent the standard deviation.

actors of those constraints are set to adequate values. It is often guaranteed that good values for these prefactors exist, but they are not necessarily a priori known [30]. Consequently, given a value of B/A , we can determine the error of the mapping in Eq. (12) as follows. On the one hand, we obtain the *highest achievable cut-value* (the number of edges connecting different sets in the partition) via an exact Max-k-Cut solver [41]. On the other hand, we determine the *cut-value of the ground state* of Eq. (12) via an exhaustive search over the spin configurations. The difference between these respective cut values is defined as the error.

Fig. 6 shows the error of Eq. (12) as a function of B/A and ζ for an arbitrary Max-3-Cut problem of 30 spins. In the white region, outlined by a green dashed line, the ground-state configuration of Eq. (12) correctly solves the COP. For the blue cells, we verified numerically that the one-hot encoding constraints (the terms of Eq. (12) with prefactor A) are violated, leading to ill-defined vertex colors. Consequently, the ground-state configuration is not a valid solution in these cells, such that the error is nonzero.

It is important to note that in Fig. 6, the range of valid B/A values is broader for $\zeta = 0.6$ compared to $\zeta = 1$. In general, as the graph size increases for $\zeta = 1$, it turns out that the mapping remains correct only for progressively smaller values of B/A , as larger

values violate the one-hot encoding constraints. Interestingly, this issue does not arise for $\zeta = 0.6$. As detailed in Supplementary Note 9, we confirmed these findings for small graphs by evaluating the error of Eq. (12) (requiring an exhaustive search as also used in Fig. 6) and extended them to larger graphs based on the strong correlation between the correctness of the mapping and the success rate.

Although decreasing B/A could theoretically eliminate mapping errors at $\zeta = 1$, this would require an unrealistic resolution of the interaction parameters, making the approach impractical. In contrast, choosing $\zeta = 0.6$ yields good performance across a much broader range of B/A values, significantly reducing sensitivity to parameter choices. Moreover, as shown in Supplementary Note 8, using $\zeta = 0.6$ generally results in similar time-to-solution (TTS) as the optimal $\zeta \in [0, 1.2]$. Hence, we conclude that setting $\zeta = 0.6$ effectively mitigates mapping errors caused by violations of the one-hot encoding constraint, without requiring impractically small values of B/A .

3.3.3 Comparison of external field implementations

Fig. 7 compares the TTS of the methods of Section 2.3 for the Max-3-Cut problems with $\zeta = 0.6$. Most data points lie in the lower right of the plots, indicating that the spin sign method solves these COPs faster. While the advantage over other methods reduces for larger problems, it generally remains the best choice. We conclude that the spin sign method also generally performs best for these Max-3-Cut problems, but that the key prerequisite for good performance is setting $\zeta \approx 0.6$.

4 Hardware considerations

In the previous section, we have shown that the spin sign method is the most effective approach to incorporate external fields in analog IMs. Additionally, it can easily be implemented in hardware using, for example, a comparator in electronic systems. Moreover, analog spin amplitudes are often measured before computing the local fields I_i [16–22]. In such

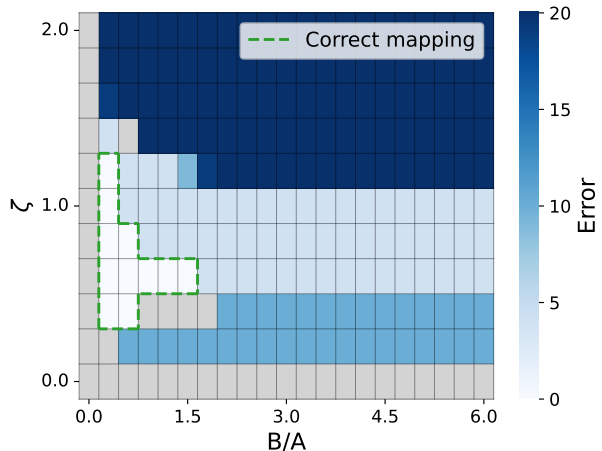


Figure 6: Error of the Max-3-Cut mapping (Eq. (12)) as a function of $\frac{B}{A}$ and ζ for the g05_10.0 graph. For every set of values $(\frac{B}{A}, \zeta)$, the ground state configuration of Eq. (12) is determined via exhaustive search. The error is defined as the difference between the cut value of this configuration and the optimal cut value (obtained via an exact solver [41]). The region where the ground-state configuration solves the Max-3-Cut problem is surrounded by a green dashed line. Grey cells indicate that the ground state is degenerate, including at least one configuration that does not solve the Max-3-Cut problem.

setups, a one-bit resolution measurement device can enforce the spin sign method, provided this only affects the local field computation and preserves the analog nature of the spins.

Whereas the spin sign method offers the best performance and can be implemented in hardware relatively easily, the mean absolute spin method performs worse and further complicates the calculation of I_i . Indeed, in addition to the standard matrix-vector multiplication, it requires computing the mean absolute spin value, which will require extending the hardware.

The auxiliary spin method, though less effective than the spin sign method, may still be useful when directly implementing external fields in hardware is challenging. However, since the auxiliary spin must

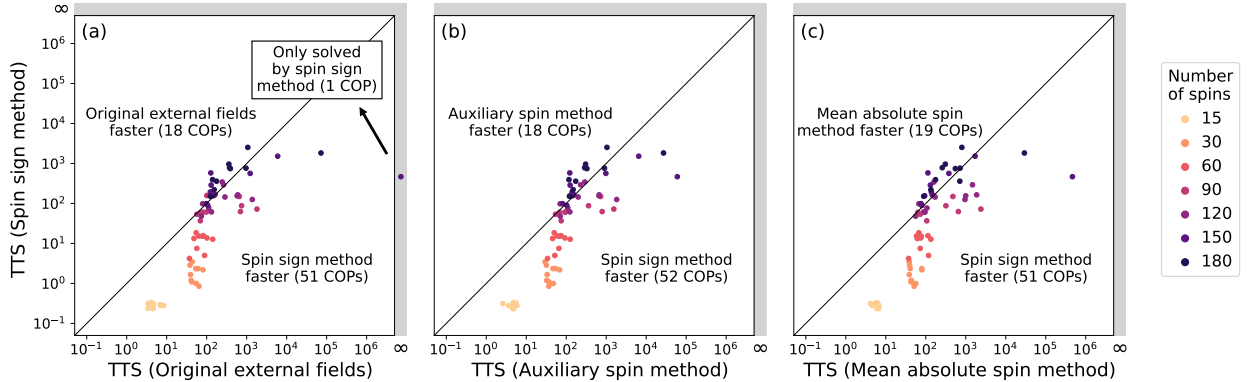


Figure 7: Comparison of time-to-solution between different methods to implement external fields for Max-3-Cut problems for $\zeta = 0.6$. The spin sign method generally solves the COPs faster than the other methods. 1 COP could not be solved using the original external fields.

connect to all spins affected by an external field, it can pose difficulties in hardware that does not allow for all-to-all coupling. Moreover, while this method is often cited as a justification for excluding external fields from hardware implementations, we emphasize that this approach is not ideal, as it leads to sub-optimal performance.

Hence, the spin sign method not only provides the best performance but is also relatively easy to implement compared to the auxiliary spin and mean absolute spin methods.

5 Conclusion

The initial implementation of external fields in IMs with analog spins, Eq. (3), is prone to imbalances in magnitude between the external fields and the spin couplings. To address this, the mean absolute spin method of Eq. (6) and the auxiliary spin method of Eq. (7) were proposed in the past.

In this work, we demonstrate that the spin sign method of Eq. (8) consistently outperforms the earlier approaches across three distinct problem classes. For SK and Beasley instances, it enables solving more COPs within the allotted time, while for Max-3-Cut, it generally achieves faster solutions than any of the other methods.

Although the spin sign method was previously shown to be effective for ballistic simulated bifurcation [31, 32], its use has remained largely confined to that setting, where \mathcal{F} in Eq. (2) is linear and spin dynamics involve momentum. It has not been widely adopted in other analog IMs [10], nor included in prior studies on balancing spin couplings and external fields [33]. In this work, we extend its application and show that it outperforms standard approaches for handling magnitude imbalances between spin couplings and external fields.

Beyond refining IM dynamics, we shed light on the embedding process of certain COPs. Contrary to some prior works, we showed that the external fields should not be rescaled with a constant $\zeta \neq 1$ for problems without soft constraints, such as SK and Beasley problems. However, we confirmed that such a rescaling can be necessary when soft constraints are used, as in Max-3-Cut. While this necessity had been observed before, we identified the underlying reason: with $\zeta = 1$, one-hot encoding constraints are often violated due to the finite resolution of interaction parameters. Choosing $\zeta \approx 0.6$ restores the embedding's correctness for the problems considered here. Notably, prior work also found this value to be optimal for one-hot encoding with more than three states [27], suggesting its robustness. Since many COPs repre-

sent multivariate variables using one-hot encoding, this insight is valuable for the Ising machine community. Moreover, since real-world COPs often involve numerous soft constraints—particularly when using IMs—it may be worthwhile to explore whether similar rescalings could benefit other types of soft constraints.

6 Data availability

The authors declare that all relevant data are included in the manuscript. Additional data are available from the corresponding author upon reasonable request.

7 Author contributions

R.D.P. and J.L. performed the simulations and wrote the manuscript. P.B., G.V.d.S., G.V. and T.V.V. supervised the project. All authors discussed the results and reviewed the manuscript.

8 Additional information

Competing interests: Guy Van der Sande is an Editorial Board Member for Communications Physics, but was not involved in the editorial review of, or the decision to publish this article. All the other authors declare no competing interests.

Acknowledgements: The authors would like to thank Ruqi Shi for generating graphs that were used to study Max-3-Cut, and Toon Sevenants for the many interesting discussions.

This research is funded by the Prometheus Horizon Europe project 101070195. It was also funded by the Research Foundation Flanders (FWO) under grants G028618N, G029519N, G0A6L25N and G006020N. Additional funding was provided by the EOS project ‘Photonic Ising Machines’. This project (EOS number 40007536) has received funding from the FWO and F.R.S.-FNRS under the Excellence of Science (EOS) programme.

References

- [1] Sean J. Weinberg, Fabio Sanches, Takanori Ide, Kazumitsu Kamiya, and Randall Correll. Supply chain logistics with quantum and classical annealing algorithms. *Scientific Reports*, 13, 2023. doi: 10.1038/s41598-023-31765-8.
- [2] Román Orús, Samuel Mugel, and Enrique Lizaso. Quantum computing for finance: Overview and prospects. *Reviews in Physics*, 4: 100028, 2019.
- [3] Alejandro Perdomo, Colin Truncik, Ivan Tubert-Brohman, Geordie Rose, and Alán Aspuru-Guzik. Construction of model hamiltonians for adiabatic quantum computation and its application to finding low-energy conformations of lattice protein models. *Physical Review A*, 78(1): 012320, 2008.
- [4] Richard Y. Li, Rosa Di Felice, Remo Rohs, and Daniel A. Lidar. Quantum annealing versus classical machine learning applied to a simplified computational biology problem. *npj Quantum Information*, 4, 2018. doi: 10.1038/s41534-018-0060-8.
- [5] Eleanor G Rieffel, Davide Venturelli, Bryan O’Gorman, Minh B Do, Elicia M Prystay, and Vadim N Smelyanskiy. A case study in programming a quantum annealer for hard operational planning problems. *Quantum Information Processing*, 14:1–36, 2015.
- [6] Florian Neukart, Gabriele Compostella, Christian Seidel, David Von Dollen, Sheir Yarkoni, and Bob Parney. Traffic flow optimization using a quantum annealer. *Frontiers in ICT*, 4:29, 2017.
- [7] Gurobi Optimization LLC. National football league scheduling. URL https://www.gurobi.com/case_studies/national-football-league-scheduling. Accessed: 2025-02-26.

- [8] Richard M Karp. Reducibility among combinatorial problems. In *50 Years of Integer Programming 1958-2008: from the Early Years to the State-of-the-Art*, pages 219–241. Springer, 2009.
- [9] Marc Mézard, Giorgio Parisi, and Miguel Angel Virasoro. *Spin glass theory and beyond: An Introduction to the Replica Method and Its Applications*, volume 9. World Scientific Publishing Company, 1987.
- [10] Naeimeh Mohseni, Peter L McMahon, and Tim Byrnes. Ising machines as hardware solvers of combinatorial optimization problems. *Nature Reviews Physics*, 4(6):363–379, 2022.
- [11] Mark W Johnson, Mohammad HS Amin, Suzanne Gildert, Trevor Lanting, Firas Hamze, Neil Dickson, Richard Harris, Andrew J Berkley, Jan Johansson, Paul Bunyk, et al. Quantum annealing with manufactured spins. *Nature*, 473(7346):194–198, 2011.
- [12] Jan Kaiser and Supriyo Datta. Probabilistic computing with p-bits. *Applied Physics Letters*, 119, 2021. doi: <https://doi.org/10.1063/5.0067927>.
- [13] Kerem Yunus Camsari, Rafatul Faria, Brian M. Sutton, and Supriyo Datta. Stochastic p-bits for invertible logic. *Phys. Rev. X*, 7:031014, 2017. doi: 10.1103/PhysRevX.7.031014.
- [14] D Pierangeli, G Marcucci, and C Conti. Large-scale photonic ising machine by spatial light modulation. *Physical review letters*, 122(21):213902, 2019.
- [15] Fuxi Cai, Suhas Kumar, Thomas Van Vaerenbergh, Xia Sheng, Rui Liu, Can Li, Zhan Liu, Martin Foltin, Shimeng Yu, Qiangfei Xia, et al. Power-efficient combinatorial optimization using intrinsic noise in memristor hopfield neural networks. *Nature Electronics*, 3(7):409–418, 2020.
- [16] Takahiro Inagaki, Yoshitaka Haribara, Koji Igarashi, Tomohiro Sonobe, Shuhei Tamate, Toshimori Honjo, Alireza Marandi, Peter L McMahon, Takeshi Umeki, Koji Enbutsu, et al. A coherent ising machine for 2000-node optimization problems. *Science*, 354(6312):603–606, 2016.
- [17] Toshimori Honjo, Tomohiro Sonobe, Kensuke Inaba, Takahiro Inagaki, Takuya Ikuta, Yasuhiro Yamada, Takushi Kazama, Koji Enbutsu, Takeshi Umeki, Ryoichi Kasahara, et al. 100,000-spin coherent ising machine. *Science advances*, 7(40):eabh0952, 2021.
- [18] Fabian Böhm, Guy Verschaffelt, and Guy Van der Sande. A poor man’s coherent ising machine based on opto-electronic feedback systems for solving optimization problems. *Nature communications*, 10(1):3538, 2019.
- [19] L. Q. English, A. V. Zampetaki, K. P. Kalinin, N. G. Berloff, and P. G. Kevrekidis. An ising machine based on networks of subharmonic electrical resonators. *Communications Physics*, 5, 2022.
- [20] Mingrui Jiang, Keyi Shan, Chengping He, and Can Li. Efficient combinatorial optimization by quantum-inspired parallel annealing in analogue memristor crossbar. *Nature communications*, 14(1):5927, 2023.
- [21] Natalia G Berloff, Matteo Silva, Kirill Kalinin, Alexis Askitopoulos, Julian D Töpfer, Pasquale Cilibrizzi, Wolfgang Langbein, and Pavlos G Lagoudakis. Realizing the classical xy hamiltonian in polariton simulators. *Nature materials*, 16(11):1120–1126, 2017.
- [22] Kirill P Kalinin and Natalia G Berloff. Global optimization of spin hamiltonians with gain-dissipative systems. *Scientific reports*, 8(1):17791, 2018.
- [23] Mastiyage Don Sudeera Hasaranga Gunathilaka, Satoshi Kako, Yoshitaka Inui, Kazushi Mimura, Masato Okada, Yoshihisa Yamamoto, and Toru Aonishi. Effective implementation of l0-regularised compressed sensing with chaotic-amplitude-controlled coherent ising machines. *Scientific Reports*, 13(1):16140, 2023.

- [24] Kazuki Ikeda, Yuma Nakamura, and Travis S Humble. Application of quantum annealing to nurse scheduling problem. *Scientific reports*, 9 (1):12837, 2019.
- [25] Tingting Zhang and Jie Han. Efficient traveling salesman problem solvers using the ising model with simulated bifurcation. In *2022 Design, Automation & Test in Europe Conference & Exhibition (DATE)*, pages 548–551. IEEE, 2022.
- [26] Abhishek Kumar Singh, Kyle Jamieson, Peter L McMahon, and Davide Venturelli. Ising machines’ dynamics and regularization for near-optimal mimo detection. *IEEE Transactions on Wireless Communications*, 21(12):11080–11094, 2022.
- [27] Hiromasa Sakaguchi, Koji Ogata, Tetsu Isomura, Shoko Utsunomiya, Yoshihisa Yamamoto, and Kazuyuki Aihara. Boltzmann sampling by degenerate optical parametric oscillator network for structure-based virtual screening. *Entropy*, 18(10):365, 2016.
- [28] Andrew D King, William Bernoudy, James King, Andrew J Berkley, and Trevor Lanting. Emulating the coherent ising machine with a mean-field algorithm. *arXiv preprint arXiv:1806.08422*, 2018.
- [29] Clayton W Commander. Maximum cut problem, max-cut. *Encyclopedia of Optimization*, 2, 2009.
- [30] Andrew Lucas. Ising formulations of many np problems. *Frontiers in physics*, 2:74887, 2014.
- [31] Hayato Goto, Kotaro Endo, Masaru Suzuki, Yoshisato Sakai, Taro Kanao, Yohei Hamakawa, Ryo Hidaka, Masaya Yamasaki, and Kosuke Tatumura. High-performance combinatorial optimization based on classical mechanics. *Science Advances*, 7(6):eabe7953, 2021.
- [32] Taro Kanao and Hayato Goto. Simulated bifurcation for higher-order cost functions. *Applied Physics Express*, 16(1):014501, 2022.
- [33] Mastiyage Don Sudeera Hasaranga Gunathilaka, Yoshitaka Inui, Satoshi Kako, Yoshihisa Yamamoto, and Toru Aonishi. Mean-field coherent ising machines with artificial zeeman terms. *J. Appl. Phys*, 134, 2023.
- [34] Angelika Wiegele. Biq mac library - a collection of max-cut and quadratic 0-1 programming instances of medium size, 2007. URL <https://biqmac.aau.at/biqmaclib.pdf>.
- [35] Giovanni Rinaldi. Rudy, a graph generator. <https://www-user.tu-chemnitz.de/~helmbert/rudy>, 1998.
- [36] Fabian Böhm, Thomas Van Vaerenbergh, Guy Verschaffelt, and Guy Van der Sande. Order-of-magnitude differences in computational performance of analog ising machines induced by the choice of nonlinearity. *Communications Physics*, 4(1):149, 2021.
- [37] Atsushi Yamamura, Hideo Mabuchi, and Surya Ganguli. Geometric landscape annealing as an optimization principle underlying the coherent ising machine. *Phys. Rev. X*, 14:031054, 2024. doi: 10.1103/PhysRevX.14.031054.
- [38] Jacob Lamers, Guy Verschaffelt, and Guy Van der Sande. Using continuation methods to analyse the difficulty of problems solved by ising machines. *Communications Physics*, 7, 2024.
- [39] Ryan Hamerly, Takahiro Inagaki, Peter L McMahon, Davide Venturelli, Alireza Marandi, Tatsuhiro Onodera, Edwin Ng, Carsten Langrock, Kensuke Inaba, Toshimori Honjo, et al. Experimental investigation of performance differences between coherent ising machines and a quantum annealer. *Science advances*, 5(5): eaau0823, 2019.
- [40] David Sherrington and Scott Kirkpatrick. Solvable model of a spin-glass. *Phys. Rev. Lett.*, 35: 1792–1796, 1975. doi: 10.1103/PhysRevLett.35.1792.
- [41] Ramin Fakhimi and Validi Hamidreza. Max k-cut. <https://github.com/qcol-lu/maxkcut>, 2022.

- [42] Mandra Salvatore, Akbari Asanjan Ata, Brady Lucas, Lott Aaron, Bernal Neira David E., and Munoz Bauza Humberto. Pysa: Fast simulated annealing in native python. URL <https://github.com/nasa/pysa>.
- [43] Moslem Noori, Elisabetta Valiante, Thomas Van Vaerenbergh, Masoud Mohseni, and Ignacio Rozada. A statistical analysis for per-instance evaluation of stochastic optimizers: How many repeats are enough? *arXiv preprint arXiv:2503.16589*, 2025.

Supplementary Material

Supplementary Note 1: Simulation of the Ising machine

Simulating a run of the Ising machine begins by drawing the initial spin amplitudes from the same Gaussian distribution as the noise (see further). Their amplitudes are updated each time step according to the Euler scheme:

$$\mathbf{s}_{t+1} = \mathbf{s}_t + \Delta t (-\mathbf{s}_t + \tanh(\alpha \mathbf{s}_t + \beta_t \mathbf{I}_t)) + \gamma \boldsymbol{\xi}_t, \quad (\text{S.1})$$

where \mathbf{s}_t is the vector of all spin amplitudes at time t , $\Delta t = 0.01$ is the Euler time step, α is the linear gain, \mathbf{I}_t is the vector of the local fields of all spin amplitudes at time t , $\gamma = 0.001$ is the noise strength and $\boldsymbol{\xi}_t$ is the vector of the noise terms of all spin amplitudes. Each noise term is drawn from a Gaussian distribution with zero mean and a standard deviation of $\sqrt{\Delta t}$. β_t is the interaction strength at time t and is given by

$$\beta_{t+1} = \beta_t + v_\beta \Delta t, \quad (\text{S.2})$$

where v_β is the annealing speed. The initial β value is β_0 and depends on the method used to implement the external fields. For the original external fields and the spin sign method, $\beta_0 = 0$ is used as the origin, i.e. all spin amplitudes equal to zero, is a fixed point only at $\beta = 0$. For the auxiliary spin method, β_0 is set to the value at which the origin undergoes its first pitchfork bifurcation, as described in Supplementary Note 4. Because computing this bifurcation point when using the mean absolute spin method is computationally expensive, we also set $\beta_0 = 0$ in that case. More details can be found in Supplementary Note 3.

The updates in Eq. (S.1) and Eq. (S.2) are repeated until either the IM obtains the target energy or $10^4/\Delta t$ updates are done.

For each problem class, the TTS was calculated for all possible combinations of parameter values within the ranges specified in Table S1 via a grid search.

The number of points per parameter in the last column determines the resolution of the sweep. The TTS mentioned in the main text is the lowest TTS obtained in this way.

As discussed in the main text, Max-3-Cut problems involve an additional parameter, B/A , which controls the relative importance of the edge constraints (weighted by B) compared to the one-hot encoding constraints (weighted by A). The term proportional to A is a sum over all vertices and therefore scales with the number of vertices N_{vert} , while the term proportional to B scales with the number of edges, i.e., $\propto N_{\text{vert}}^2$. Consequently, the same relative importance between constraints is achieved at lower values of B/A as N_{vert} increases. Since we use a fixed number of sampling points (7) in our parameter scan, we rescale the range of B/A with $1/N_{\text{vert}}$ to ensure that the scanned values remain relevant and adequately capture the region of interest for each value of N_{vert} .

Supplementary Note 2: Initial search direction without rescaling of the external fields

When using the original external fields method of Eq. 3 of the main paper, the time evolution of the spin amplitudes when using the tanh nonlinearity is given by

$$\frac{ds_i}{dt} = -s_i + \tanh \left(\alpha s_i + \beta \left(\sum_j J_{ij} s_j + h_i \right) \right). \quad (\text{S.3})$$

When $\beta = 0$, the origin (all spin amplitudes equal to zero) is a fixed point of the system. We are now interested in the state that emerges when β is slightly

Table S1: Parameter sweeps. The ranges of the hyperparameters used to determine their optimal values.

Problem class	Parameter name	Lowest value	Highest value	Spacing type	Number of points
SK	α	-10	1	Linear	12
	v_β	10^{-5}	10^{-1}	Log (base 10)	5
	ζ	0	2	Linear	11
Beasley	α	-10	1	Linear	12
	v_β	10^{-5}	10^{-1}	Log (base 10)	5
	ζ	0	2	Linear	11
Max-3-Cut	α	-10	1	Linear	5
	v_β	10^{-5}	10^{-1}	Log (base 10)	5
	ζ	0	1.2	Linear	7
	B/A	0	$60/N_{\text{vert}}$	Linear	7

increased. This means that at a fixed point, for all i

$$\beta = \frac{-\alpha s_i + \tanh^{-1}(s_i)}{\sum_j J_{ij} s_j + h_i}. \quad (\text{S.4})$$

The partial derivative with respect to s_k , evaluated at the origin is given by

$$\left. \frac{\partial \beta}{\partial s_k} \right|_{\mathbf{s}=\mathbf{0}, \beta=0} = \frac{1-\alpha}{h_k}. \quad (\text{S.5})$$

Since Eq. (S.4) is invertible for $\alpha < 1$, we can write:

$$\left. \frac{\partial s_k}{\partial \beta} \right|_{\mathbf{s}=\mathbf{0}, \beta=0} = \frac{h_k}{1-\alpha}. \quad (\text{S.6})$$

This means that, when starting from the origin and increasing β , the system will evolve in a direction proportional to the external field h_i , independent of the values of the spin couplings J_{ij} .

Supplementary Note 3: Bifurcation of the mean absolute spin method

In general, the stability of a fixed point is related to the eigenvalues of the Jacobian matrix evaluated at

that fixed point. When all eigenvalues are negative, the fixed point is stable. When one eigenvalue becomes positive, the fixed point becomes unstable in the direction of the corresponding eigenvector.

When using the mean absolute spin method in combination with the tanh nonlinearity, the evolution of the spin amplitudes is given by:

$$\frac{ds_i}{dt} = -s_i + \tanh \left(\alpha s_i + \beta \left(\sum_j J_{ij} s_j + h_i \frac{1}{N} \sum_k |s_k| \right) \right). \quad (\text{S.7})$$

The origin bifurcates when its stability changes, i.e. when the largest eigenvalue of the Jacobian matrix goes through zero and becomes positive. The Jacobian matrix evaluated at the origin is given by

$$\begin{aligned} \mathcal{U}_{il} \Big|_{\mathbf{s}=\mathbf{0}} &= - \left. \frac{\partial \frac{ds_i}{dt}}{\partial s_l} \right|_{\mathbf{s}=\mathbf{0}} \\ &= (\alpha - 1) \delta_{il} + \beta J_{il} + \beta \frac{h_l}{N} \lim_{s_l \rightarrow 0} \text{sign}(s_l), \end{aligned} \quad (\text{S.8})$$

where δ_{il} is the Kronecker delta. So, the Jacobian matrix when using the mean absolute spin method is discontinuous at the origin. This means that, in each of the 2^N directions around the origin, the Jacobian has different eigenvalues and eigenvectors. Therefore, to locate the bifurcation point of the origin, one must substitute the signs of the spins of all directions in

Eq. (S.8) and determine whether the principal eigenvector has the same signs. The origin will bifurcate in the direction of such an eigenvector with the eigenvalue that first becomes positive. Because of this, determining the β value of the bifurcation point of the origin when using the mean absolute spin method is computationally more demanding than finding the ground state by a brute force search, which defeats the purpose of using an Ising machine.

As the bifurcation point cannot be easily found, the annealing technique is initialized at $\beta_0 = 0$. At this point, however, the origin is still stable in all directions and the spin amplitudes will just remain at zero. The spin amplitudes will only deviate from zero when β has been annealed to a value high enough so that the origin is unstable in at least one direction. This means that the inability to analytically calculate the bifurcation point of the mean absolute spin method leads to wasted simulation time and therefore a slightly inflated TTS.

While it is, in principle, possible to develop a heuristic to estimate an approximate β_0 for the mean absolute spin method—potentially improving its performance—we do not pursue that direction here. Instead, we consider a complementary scenario: setting $\beta_0 = 0$ for the auxiliary spin method, rather than using the value defined in Eq. (S.13) (the latter equation is used to obtain the results in the main text). This intentionally introduces an amount of wasted simulation time, similar to that of the mean absolute spin method, allowing us to assess the impact of β_0 on the TTS of the IM.

Fig. S1 illustrates this scenario for (a) SK problems, (b) Beasley problems, and (c) Max-3-Cut problems. It mirrors Figures 2(b), 3(b), and 7(b) from the main text, but with the data shifted horizontally to the right to reflect the new initialization at $\beta_0 = 0$ for the auxiliary spin method. Comparing Fig. S1 with the original figures, we find that this shift modestly affects the SK problem data, while its impact on the Beasley and Max-3-Cut problems is negligible. Importantly, even for the SK problems, the shift is small enough that it does not alter the relative performance between methods shown in Fig. 2 of the main text. From these observations we conclude that setting $\beta_0 = 0$ for the mean absolute spin method is

not the main cause of the lower performance of this method.

Supplementary Note 4: Bifurcation of the auxiliary spin method

When using the auxiliary spin method in combination with the tanh nonlinearity, the evolution of the spin amplitudes is given by:

$$\frac{ds_i}{dt} = -s_i + \tanh\left(\alpha s_i + \beta \sum_j J'_{ij} s_j\right), \quad (\text{S.9})$$

where \mathbf{J}' is the extended interaction matrix introduced in section 2.3.3 of the main text. The Jacobian matrix evaluated at the origin is given by

$$\mathcal{U}_{il} \Big|_{\mathbf{s}=\mathbf{0}} = -\frac{\partial \frac{ds_i}{dt}}{\partial s_l} \Big|_{\mathbf{s}=\mathbf{0}} = (\alpha - 1)\delta_{il} + \beta J'_{il}. \quad (\text{S.10})$$

The eigenvalues of this matrix λ_i are given by

$$\lambda_i = \alpha - 1 + \beta \mu_i, \quad (\text{S.11})$$

where μ_i are the eigenvalues of the extended interaction matrix \mathbf{J}' . When all eigenvalues λ_i are negative, the origin is stable. When one eigenvalue λ_i becomes positive, the origin becomes unstable in the direction of the corresponding eigenvector. This happens when

$$\lambda_+ = 0 = \alpha - 1 + \beta \mu_+ \quad (\text{S.12})$$

$$\beta = \frac{1 - \alpha}{\mu_+}, \quad (\text{S.13})$$

where μ_+ is the largest eigenvalue of the extended interaction matrix \mathbf{J}' .

Supplementary Note 5: PySA operation

The PySA algorithm performs simulated annealing with parallel tempering on n_{replicas} replicas at different temperatures. These replicas are initialized in random states and at a temperature given by

$$T_k = \begin{cases} T_{\min} R^{k-1} & k = 1, \dots, n_{\text{replicas}} - 1 \\ 0 & k = n_{\text{replicas}} \end{cases}$$

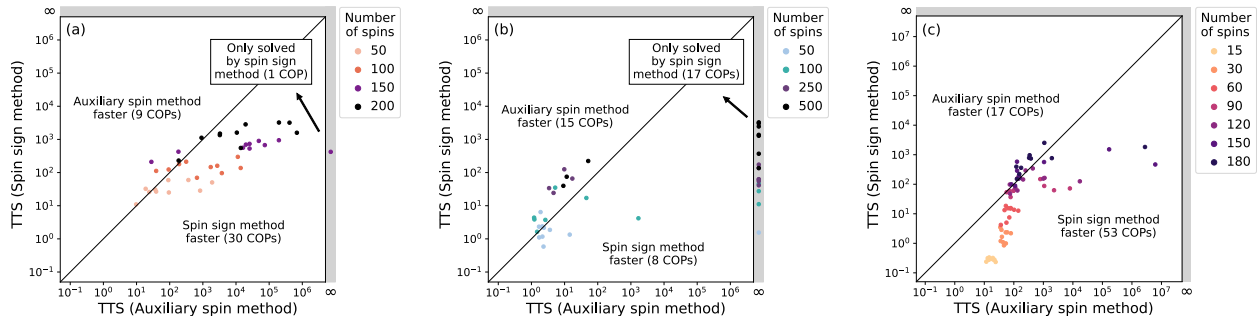


Figure S1: Comparison of time-to-solution between the auxiliary spin method and the spin sign method for (a) SK problems, (b) Beasley problems, and (c) Max-3-Cut problems. These plots replicate Figures 2(b), 3(b), and 7(b) from the main text, but with the auxiliary spin method initialized at $\beta_0 = 0$ instead of the value given in Eq. (S.13). Comparison with the original figures shows that the choice of β_0 has a limited effect on the TTS and does not alter the relative performance between methods.

where T_k is the temperature of replica k and R is given by

$$R = \exp\left(\frac{1}{n_{\text{replicas}} - 2} \log\left(\frac{T_{\text{max}}}{T_{\text{min}}}\right)\right).$$

So, there is one replica at temperature zero and the other replicas have temperatures distributed between T_{min} and T_{max} .

The replicas are then updated in sweeps. In our case, a sweep consists of attempting a spin flip for each spin in random order. In total n_{sweeps} are performed for each replica.

This procedure of initializing and performing sweeps is repeated n_{reads} times.

In order to search for the ground state energies of the Sherrington-Kirkpatrick (SK) spin glasses, the algorithm was run five times, using different values for the parameters. The values of these parameters can be found in Table S2. This resulted in the same energies that were obtained by the Ising machine simulations for problems of 100 and 150 spins. However, for the problems with 200 spins, the Ising machine found equal or lower energies than PySA.

Table S2: PySA parameters. Parameter values used to search for the ground state energy of SK problems.

Run	n_{sweeps}	n_{replicas}	n_{reads}	T_{min}	T_{max}
1	100	5000	1000	0.01	3.0
2	1000	500	1000	0.01	3.0
3	500	500	1000	0.001	6.0
4	500	1000	500	0.001	10.0
5	500	1000	800	0.001	15.0

Supplementary Note 6: Optimal ζ for SK and Beasley problems

As discussed in section 2 of the main text, setting $\zeta = 1$ guarantees that the ground state of the binary Hamiltonian solves the original COP. This guarantee is lost for $\zeta \neq 1$. However, small deviations from $\zeta = 1$ can still be expected to provide valid solutions in many cases. Moreover, adding ζ as an additional tunable parameter cannot deteriorate the performance. Figs. S2 and S3 examine whether such improvements are practically meaningful. Fig. S2 compares the TTS obtained using an optimized ζ with the TTS using fixed $\zeta = 1$ for SK problems; Fig. S3 shows the same comparison for Beasley instances. In both

cases, when methods other than the original external fields are used, most data points lie close to the diagonal, indicating that optimizing ζ leads to minimal improvement in TTS. This effect is most pronounced for the spin sign method.

Supplementary Note 7: Transformation from binary spins to bipolar spins

When solving the Beasley instances of the BiqMac library, the goal is to find the configuration of binary spins $x_i \in \{0, 1\}$ that minimizes $\mathbf{x}^T \mathbf{Q} \mathbf{x}$, with \mathbf{Q} a symmetric matrix.

This problem can be rewritten in terms of bipolar spins $\sigma_i \in \{-1, 1\}$ using the transformation

$$x_i = \frac{\sigma_i + 1}{2}. \quad (\text{S.14})$$

The objective function now becomes

$$\begin{aligned} \sum_{ij} Q_{ij} x_i x_j &= \sum_{ij} Q_{ij} \frac{\sigma_i + 1}{2} \frac{\sigma_j + 1}{2} \\ &= \frac{1}{4} \sum_{ij} Q_{ij} (\sigma_i \sigma_j + \sigma_i + \sigma_j + 1). \end{aligned} \quad (\text{S.15})$$

$$(\text{S.16})$$

Using that \mathbf{Q} is symmetric

$$\sum_{ij} Q_{ij} \sigma_i = \sum_{ij} Q_{ji} \sigma_j = \sum_{ij} Q_{ij} \sigma_j, \quad (\text{S.17})$$

We can rewrite the objective function with the following definitions: $J_{ij} := -\frac{1}{2} \tilde{Q}_{ij}$ and $h_i := -\frac{1}{2} \sum_j Q_{ij}$, where $\tilde{\mathbf{Q}}$ is the same as \mathbf{Q} , but with the diagonal elements set to zero.

$$-\frac{1}{2} \sum_{ij} J_{ij} \sigma_i \sigma_j - \sum_i h_i \sigma_i. \quad (\text{S.18})$$

Here, we neglected the constant term and the diagonal elements of the interaction matrix, as they are of no importance when minimizing the objective function.

Note that the problem in terms of binary spins does not have any external fields, but the same problem in terms of bipolar spins does.

When tackling Max-3-Cut problems, a similar procedure can be applied. The Hamiltonian of such problems is given by

$$\mathcal{H} = A \sum_{v \in V} \left(1 - \sum_{i=1}^3 x_{v,i} \right)^2 + B \sum_{(uv) \in E} \sum_{i=1}^3 x_{u,i} x_{v,i}, \quad (\text{S.19})$$

This can again be rewritten in terms of bipolar spins by using the transformation of Eq. (S.14).

$$\begin{aligned} \mathcal{H} &= A \sum_{v \in V} \left(1 - \sum_{i=1}^3 \frac{\sigma_{v,i} + 1}{2} \right)^2 \\ &\quad + B \sum_{(uv) \in E} \sum_{i=1}^3 \frac{\sigma_{u,i} + 1}{2} \frac{\sigma_{v,i} + 1}{2}. \end{aligned}$$

We can rewrite the first term as follows:

$$\begin{aligned} &A \sum_{v \in V} \left(1 - \sum_{i=1}^3 \frac{\sigma_{v,i} + 1}{2} \right)^2 \\ &= A \sum_{v \in V} \left(1 + \left(\sum_{i=1}^3 \frac{\sigma_{v,i} + 1}{2} \right)^2 - 2 \sum_{i=1}^3 \frac{\sigma_{v,i} + 1}{2} \right) \\ &= A \sum_{v \in V} \left(\sum_{i,j=1}^3 \frac{\sigma_{v,i} \sigma_{v,j}}{4} + \sum_{i=1}^3 \frac{\sigma_{v,i}}{2} + \frac{1}{4} \right). \end{aligned}$$

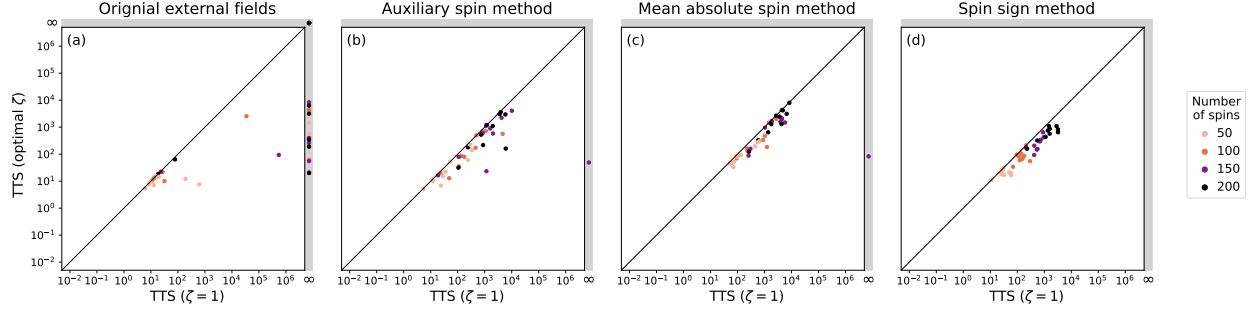


Figure S2: Comparison of time-to-solution between $\zeta = 1$ and the optimal ζ that minimizes the TTS, for SK problems. In Fig. (a), 6 data points coincide in the grey area in the top right. The corresponding COPs could not be solved with $\zeta = 1$, nor with optimal ζ (i.e. $TTS = \infty$, $SR = 0\%$), given the allocated compute time of $t = 10^4$.

The second term can be rewritten as

$$\begin{aligned}
& B \sum_{(uv) \in E} \sum_{i=1}^3 \frac{\sigma_{u,i} + 1}{2} \frac{\sigma_{v,i} + 1}{2} \\
&= B \sum_{(uv) \in E} \sum_{i=1}^3 \left(\frac{\sigma_{u,i} \sigma_{v,i}}{4} + \frac{1}{4} \right) \\
&\quad + B \sum_{(uv) \in E} \sum_{i=1}^3 \left(\frac{\sigma_{u,i}}{4} + \frac{\sigma_{v,i}}{4} \right) \\
&= B \sum_{(uv) \in E} \sum_{i=1}^3 \left(\frac{\sigma_{u,i} \sigma_{v,i}}{4} + \frac{1}{4} \right) \\
&\quad + B \sum_{v \in V} \sum_{i=1}^3 \frac{\sigma_{v,i}}{4} \deg(v)
\end{aligned}$$

where in the last line, we changed the sum of the second term from going over all edges of the graph, to going over all vertices. This, while once again ignoring all constant terms gives

$$\begin{aligned}
\mathcal{H} &= \frac{A}{4} \sum_{v \in V} \sum_{i \neq j} \sigma_{v,i} \sigma_{v,j} + \frac{B}{4} \sum_{(uv) \in E} \sum_{i=1}^3 \sigma_{u,i} \sigma_{v,i} \\
&\quad + \sum_{v \in V} \sum_{i=1}^3 \left(\frac{A}{2} + \frac{B}{4} \deg(v) \right) \sigma_{v,i},
\end{aligned} \tag{S.20}$$

Supplementary Note 8: Optimal ζ for Max-3-Cut problems

As explained in the main text, the optimal ζ value for Max-3-Cut problems converges to 0.6 as the problem size increases. While there is some variation on this problem-specific optimal ζ value, using $\zeta = 0.6$ yields comparable performance across all problems and methods of implementing the external fields. Fig. S4 compares the time-to-solution (TTS) achieved using the optimized value of ζ (vertical axis) versus a fixed value of ζ (horizontal axis) for all Max-3-Cut problem instances. Each row corresponds to a different fixed value: $\zeta = 0.4$, $\zeta = 0.6$, and $\zeta = 0.8$ and each column represents one of the four methods considered to implement external fields. In these plots, each point represents a single problem instance. Points lying on the diagonal indicate that either the fixed value of ζ is the instance-specific optimal value or that it has a similar performance. Notably, for $\zeta = 0.6$, the majority of points cluster tightly around the diagonal across all methods, suggesting that this choice often yields near-optimal performance. In contrast, for $\zeta = 0.4$ and $\zeta = 0.8$, many points fall noticeably below the diagonal, indicating that fixing ζ to these values more frequently results in suboptimal performance.

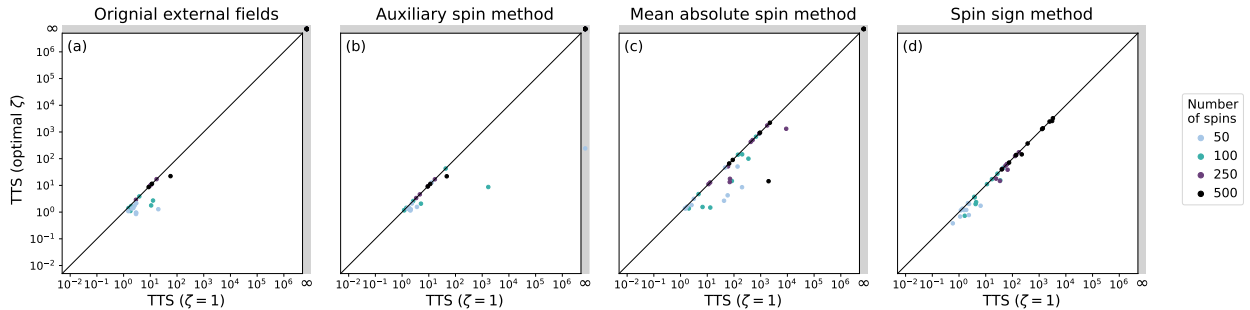


Figure S3: Comparison of time-to-solution between $\zeta = 1$ and the optimal ζ that minimizes the TTS, for each of the methods, for Beasley problems. If COPs could not be solved with $\zeta = 1$, nor with optimal ζ (i.e. $TTS = \infty$, $SR = 0\%$), given the allocated compute time of $t = 10^4$, then they appear in the grey area at the top right. These data points coincide. The number of such COPs in Fig. (a)–(d) is 17, 16, 5, and 0, respectively.

Supplementary Note 9: Extending the connection between ζ and the embedding validity to larger problems

Due to limited computational resources, it is not feasible to generate mapping-correctness plots like Fig. 6 from the main text for systems larger than 30 spins. However, as the IM is only expected to perform well when the mapping is correct, regions of high success rate can serve as a proxy for identifying regions of valid mapping. As illustrated in Fig. S5, the success rate under slow annealing conditions strongly correlates with the correct-mapping region identified in Fig. 6 of the main text. Notably, using $\zeta = 0.4$ or $\zeta = 0.6$ allows for a broader range of B/A values that yield high success rates. To quantify this trend, Fig. S6 shows the fraction of tested B/A values (defined in Table S1) that result in success rates larger than 10% as a function of system size. The figure reveals that this fraction shrinks with increasing problem size for $\zeta = 1$, while such a strong decrease is not observed for $\zeta = 0.6$. Even though these figures are made using the original external fields, the conclusions also hold for the other methods, as the mapping correctness is independent of the method of implementing the external field. Moreover, the con-

clusions also hold when varying the arbitrary threshold of 10% success rate.

Supplementary Note 10: optimal working point for the spin sign method.

Figs. S7 to S9 present the success rate, TTS, and average runtime T of successful runs for all problem instances. Fig. S7 corresponds to the SK instances, where the number following “N” in the label indicates the number of spins. Figs. S8 and S9 report results for the Beasley and Max-3-Cut problems, respectively, using the BiqMac naming convention.

Across these figures, the spin-sign method often exhibits substantially lower success rates than the other three methods. However, its significantly shorter average runtime frequently results in superior TTS performance. This is because, when optimizing for TTS, the hyperparameter optimization tends to favor scenarios in which the spin-sign method rapidly converges, albeit with lower success probabilities, leading to a lower overall TTS. This type of operation is sometimes referred to as *fail fast mode* [43]. Note that it is more often observed for smaller problem sizes. For larger problems, T tends to be more similar between all methods.

It is also important to note that the spin-sign method does not universally underperform in terms of success rate. While its success rates can be lower when performing a hyperparameter optimization that minimizes TTS, this is a consequence of favoring fast-converging configurations rather than a fundamental limitation of the method. In fact, several instances are solvable only with this method, while the others fail. Furthermore, as shown in Fig. S10, when the hyperparameters are optimized to maximize success rate instead of TTS, the spin-sign method operates in a regime with consistently higher success rates than before, often comparable to or higher than those of the other methods.

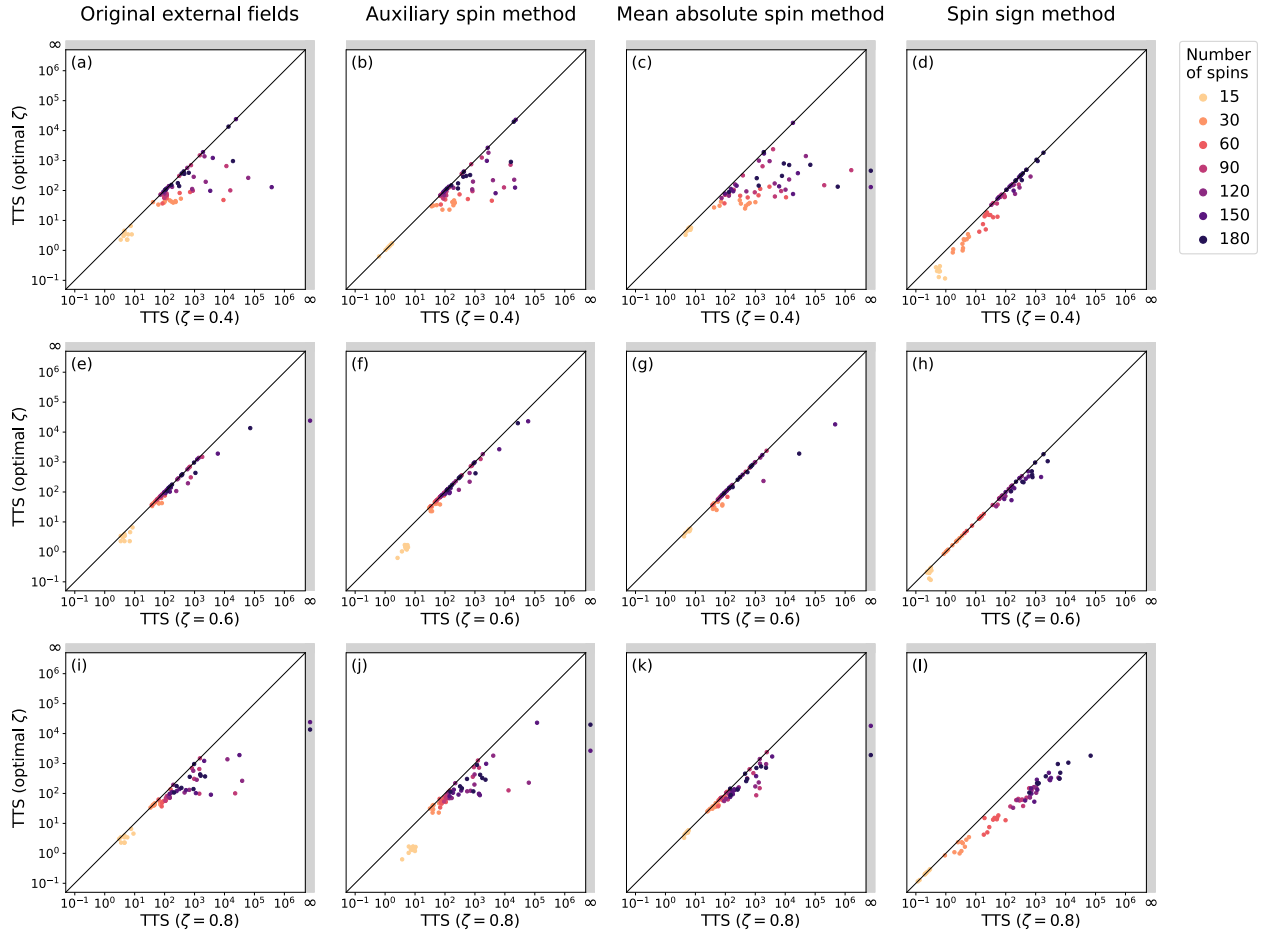


Figure S4: Comparison of the TTS achieved with optimized ζ values versus fixed $\zeta \in \{0.4, 0.6, 0.8\}$ for Max-3-Cut instances. Each column corresponds to one of the four methods to implement the external fields. The vertical axis always shows the TTS obtained using the optimal ζ per instance, while the horizontal axis shows the TTS with a fixed $\zeta \in \{0.4, 0.6, 0.8\}$. Each point represents a single problem instance. Points lying on the diagonal indicate equal performance between fixed and optimized ζ .

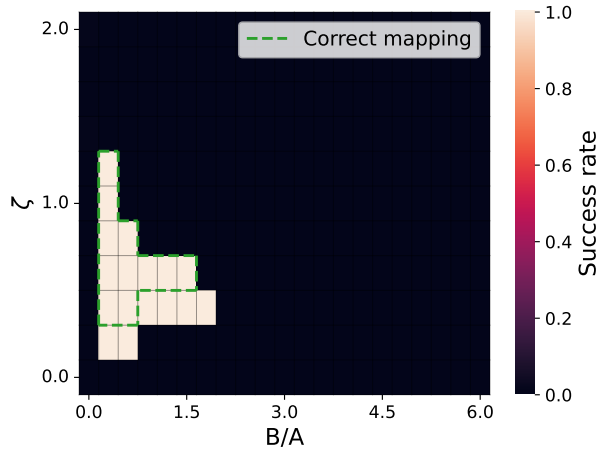


Figure S5: Correlation between success rate and correct mapping. Success rate of the g05_10.0 graph when rescaling the external fields with a constant ζ , as a function of ζ and B/A when slow annealing is performed ($d\beta/dt = 0.001$). No dynamic rescaling factor is applied. Other parameters are set as follows: $\alpha = -1$, $\gamma = 0.001$, $n_{\text{init}} = 100$.

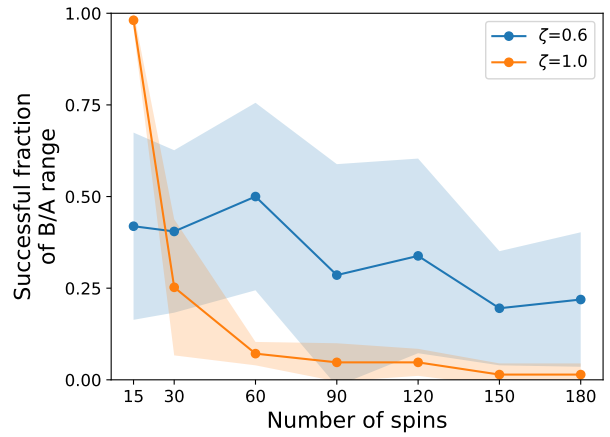


Figure S6: Fraction of valid B/A values. Fraction of the tested B/A values (defined in Table S1) for which the success rate exceeds an arbitrary threshold of 10% as a function of the number of spins. Each dot represents the mean value across 10 Max-3-Cut problems. Shaded areas represent the standard deviation. The underlying simulations were performed for the original external fields method, $\alpha = -1$, and $\frac{d\beta}{dt} = 0.001$.

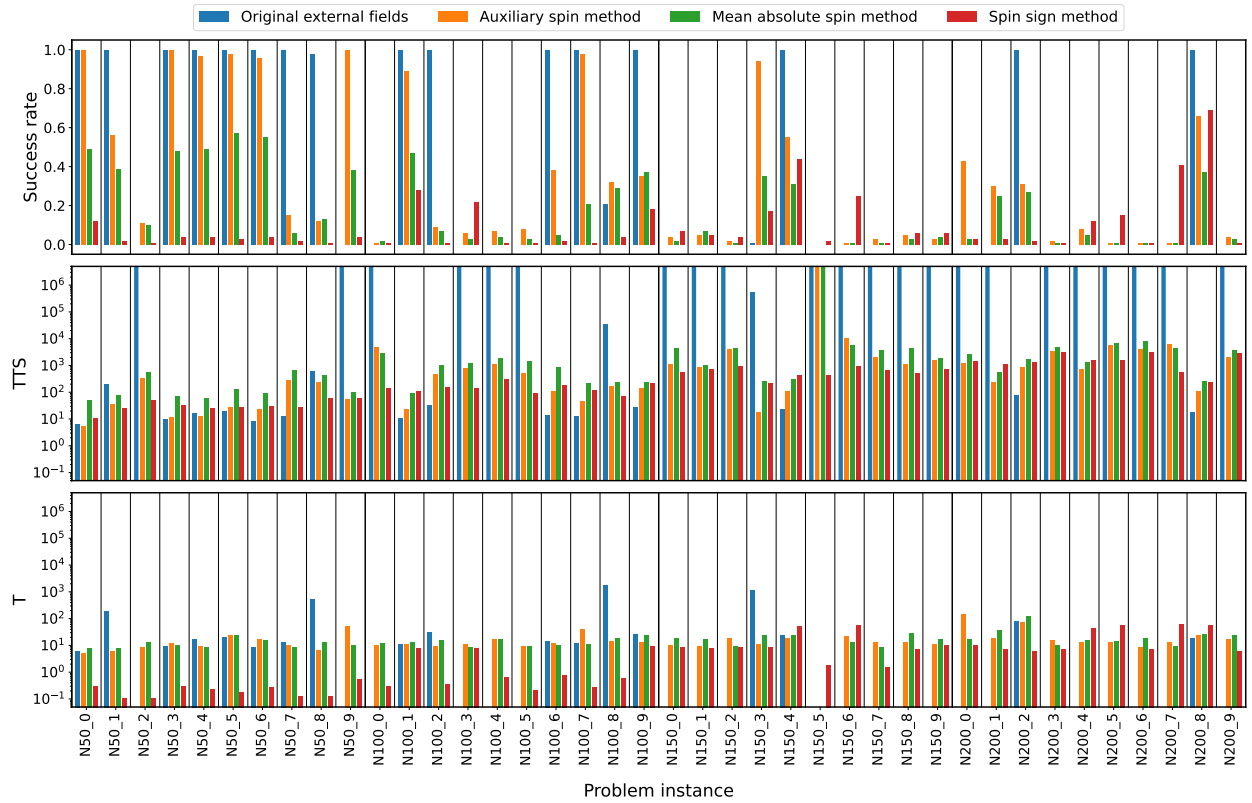


Figure S7: Performance for SK problems. For every SK problem instance and for every implementation method for the external fields, the values of α and v_β are determined that minimize TTS. For those values of the hyperparameters, the success rate, time-to-solution (TTS), and average runtime T of successful runs is shown. TTS bars that reach the upper edge denote TTS= ∞ .

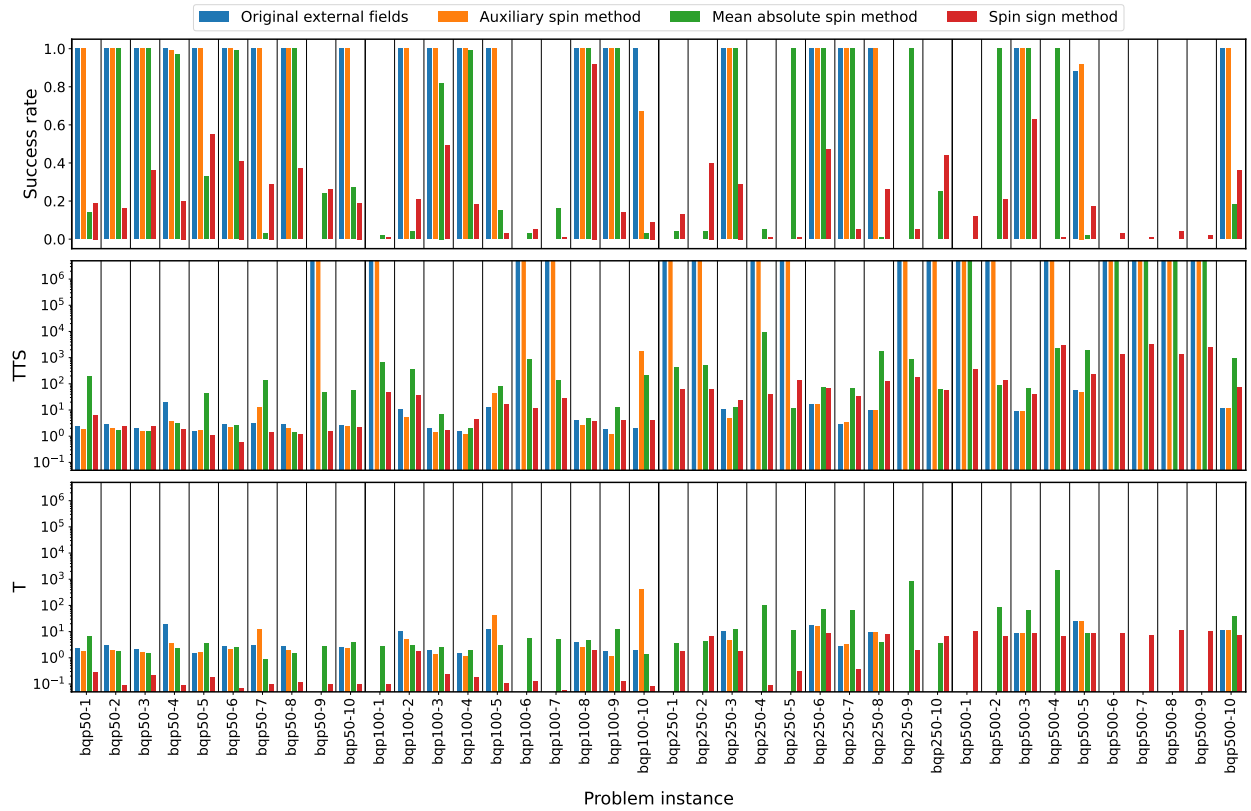


Figure S8: Performance for Beasley problems. For every Beasley problem instance and for every implementation method for the external fields, the values of α and v_β are determined that minimize TTS. For those values of the hyperparameters, the success rate, time-to-solution (TTS), and average runtime T of successful runs is shown. TTS bars that reach the upper edge denote TTS= ∞ .

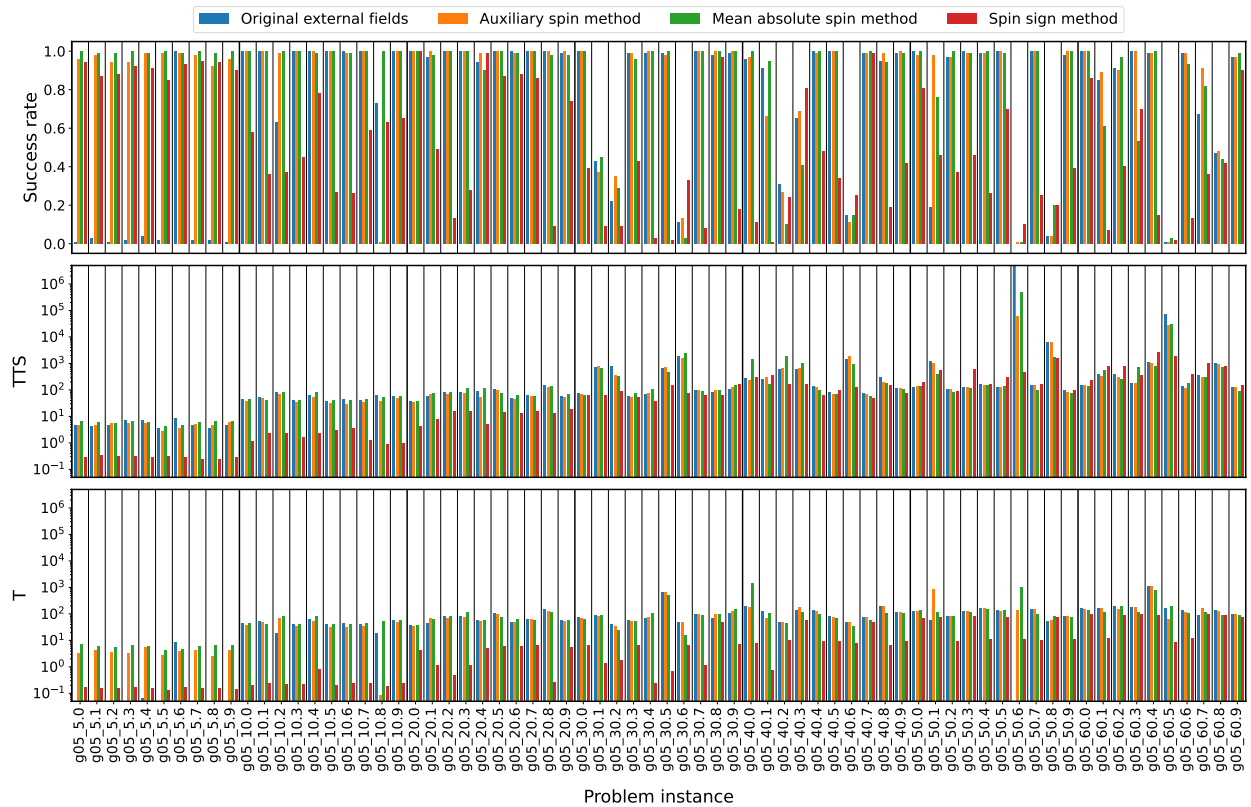


Figure S9: Performance for Max-3-Cut problems. For every Max-3-Cut problem instance and for every implementation method for the external fields, the values of α and v_β are determined that minimize TTS. For those values of the hyperparameters, the success rate, time-to-solution (TTS), and average runtime T of successful runs is shown. TTS bars that reach the upper edge denote TTS= ∞ .

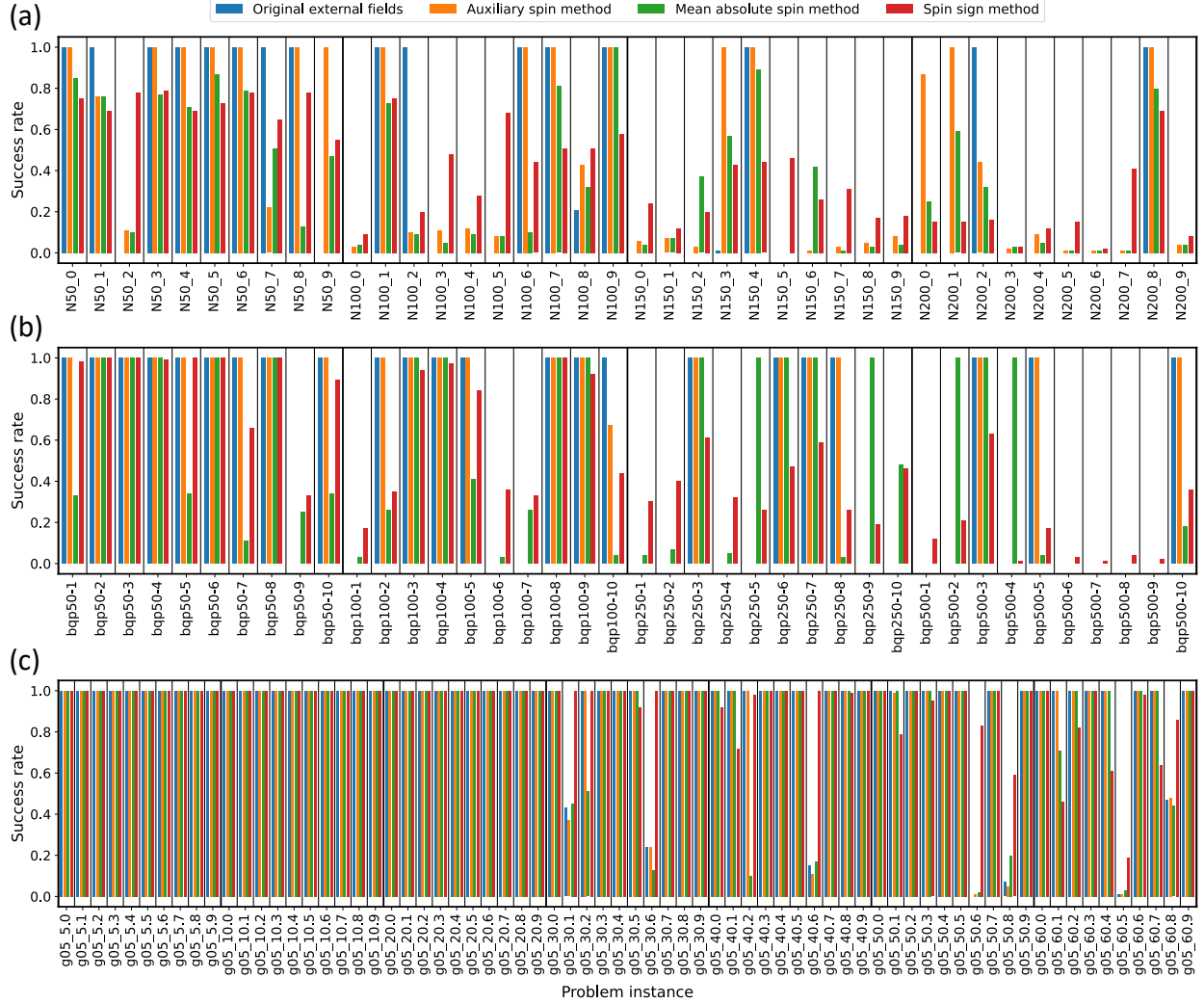


Figure S10: Performance for all problems when prioritizing success rate. Results with hyperparameters chosen to maximize success rate. This contrasts with the main text, where hyperparameters are chosen to minimize TTS. Panels (a) and (b) show $\max_{\alpha, v, \beta}$ SR for SK and Beasley problems, respectively, with $\zeta = 1$. Panel (c) shows $\max_{\alpha, v, \beta, \frac{B}{A}}$ SR for Max-3-Cut problems, with $\zeta = 0.6$.